







Pressure-induced band-gap energy increase in a metal iodate

Akun Liang ¹, Lan-Ting Shi,² Robin Turnbull,¹ Francisco Javier Manjón ³, Jordi Ibáñez ⁴, Catalin Popescu,⁵ M. Jasmin ⁶, Jaspreet Singh,⁷ Kanchana Venkatakrishnan,⁷ Ganapathy Vaitheeswaran ⁸, and Daniel Errandonea ^{1,*}

¹*Departamento de Física Aplicada—ICMUV, Universitat de València, MALTA Consolider Team, Edificio de Investigación, c/ Dr. Moliner 50, 46100 Burjassot, Valencia, Spain*

²*Institute of High Energy Physics, Chinese Academy of Sciences (CAS), 100049 Beijing, China*

³*Instituto de Diseño para la Fabricación y Producción Automatizada, MALTA Consolider Team, Universitat Politècnica de València, Camí de Vera s/n, 46022 València, Spain*

⁴*Geosciences Barcelona (GEO3BCN), Malta Consolider Team, CSIC, 08028 Barcelona, Spain*

⁵*CELLS-ALBA Synchrotron Light Facility, Cerdanyola, 08290 Barcelona, Spain*

⁶*TKM College of Arts and Science, 691005 Kerala, India*

⁷*Department of Physics, Indian Institute of Technology Hyderabad, Kandi-502285, Sangareddy, Telangana, India*

⁸*School of Physics, University of Hyderabad, Prof. C. R. Rao Road, Gachibowli, Hyderabad 500046, Telangana, India*



(Received 5 October 2022; revised 16 November 2022; accepted 29 November 2022; published 9 December 2022)

A wide band gap is one of the essential requirements for metal iodates to be used as nonlinear optical materials. Usually, the band gap of these materials decreases under the application of pressure. Herein, we introduce a case in which the band-gap energy of a hydrated metal iodate, namely $\text{Ca}(\text{IO}_3)_2 \cdot \text{H}_2\text{O}$, has been successfully increased, from 4.52 to 4.92 eV, by applying external pressure without showing signs of saturation upon increasing pressure. The pressure-induced nonlinear band-gap opening correlates with the pressure-induced shortening of the I-O bond distances, as obtained from x-ray diffraction measurements. In addition, two pressure-induced isostructural phase transitions are observed in the pressure regions of 6.6–8.0 and 13.0–15.5 GPa. These two isostructural phase transitions cause a nonlinear pressure-induced evolution of the band-gap energy and crystal lattice parameters, as well as the occurrence of several extra peaks and peak splitting in Raman spectra.

DOI: [10.1103/PhysRevB.106.235203](https://doi.org/10.1103/PhysRevB.106.235203)

I. INTRODUCTION

Due to the existence of the stereochemically active lone electron pairs and the nonzero dipole moment in the iodate group, $[\text{IO}_3]^-$, iodates of metals (known as metal iodates) typically crystallize with noncentrosymmetric crystal structures and exhibit a large second-harmonic generation response [1]. By carefully designing and manipulating the orientation of the polar units, it is possible to synthesize metal iodates with an ultrahigh second-harmonic generation response. For example, the second-harmonic generation responses of $\text{BaNbO}(\text{IO}_3)_5$ and $\text{LiMg}(\text{IO}_3)_3$ are respectively about 14 and 24 times larger than that of KH_2PO_4 , the most widely used second-order nonlinear optical material [2,3].

In order to be successfully implemented as nonlinear optical materials, a compound needs to have (i) a large second-harmonic generation response; (ii) a moderate birefringence; (iii) a wide transparency region; (iv) a high laser damage threshold; and (v) a good chemical stability. The large second-harmonic generation response is needed for a highly efficient laser conversion and the moderate birefringence for an optimized phase matching. The wide transparency region (large band gap) is needed to allow the converted laser light to exit the nonlinear optical crystal without being absorbed by promoting electrons from the valence band to the conduction

band. Finally, the good chemical stability is needed for practical applications and the high laser damage threshold (also related to a large band gap) is needed to avoid damage of the nonlinear optical material by laser irradiation. In summary, a wide band-gap energy is essential for the implementation of metal iodates as nonlinear optical materials.

As our previous studies have shown, there are two important factors to consider in the design of wide band-gap metal iodates [4,5]: (i) Avoiding the use of partially filled transition metals, because the $3d$ state of the partially filled metal will contribute to either the valence band maxima or the conduction band minima, and thus narrow the band-gap energy [5]. Some partially filled $3d$ states with appropriate coordination can also exhibit photoabsorption related to internal $d-d$ transitions [6]. (ii) Minimizing the I-O bond distance, because there is an inversely proportional relationship between the band-gap energy and the I-O bond distance in nontransition metal or closed-shelled transition metal iodates [4]. This means that shortening the I-O bond distance increases the band-gap energy of metal iodates.

Pressure is an efficient and clean external parameter for manipulating the interatomic distances in materials and, therefore, also for tuning the band-gap energy. Indeed, we have found that the band-gap energies of $\text{Zn}(\text{IO}_3)_2$ [4], $\text{Mg}(\text{IO}_3)_2$ [4], $\text{Fe}(\text{IO}_3)_3$ [5], and $\text{Co}(\text{IO}_3)_2$ [6], all decrease under compression. Moreover, we have demonstrated a relation between the decrease of the band gap with pressure in those compounds and the pressure dependence of their I-O bond

*Corresponding author: daniel.errandonea@uv.es

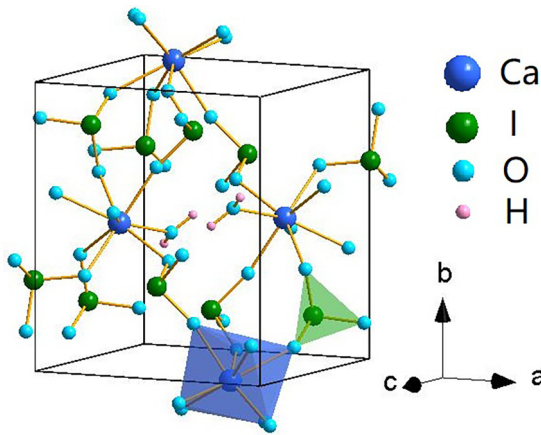


FIG. 1. Crystal structure of $\text{Ca}(\text{IO}_3)_2 \cdot \text{H}_2\text{O}$ at ambient pressure.

distances. Since the crystal structures of each of these four metal iodates share the similar feature of layers containing IO_3 pyramids, and since all the IO_3 units are aligned in a parallel manner, in all four of these iodates the average bond distance between I and the three nearest neighbor O atoms expands under compression due to the pressure-induced approach of the three next-nearest O atoms from the neighboring IO_3 layer. Therefore, in the case of the four previously studied metal iodates, pressure shortens the large I-O next-nearest-neighbor bond distance while enlarging the shorter I-O nearest-neighbor distance. This enlargement of the short I-O bond distances causes the narrowing of the band-gap energy with increasing pressure in the four aforementioned metal iodates.

The above result suggests that if pressure is applied on nontransition or closed-shell transition metal iodates, in which not all IO_3 units are aligned along the same direction, the I-O bond distances could be shortened by external pressure and the band-gap energy could be opened as pressure increases. Consequently, we chose $\text{Ca}(\text{IO}_3)_2 \cdot \text{H}_2\text{O}$ to perform this high-pressure study of a nontransition metal iodate. The hydrated calcium iodate crystallizes in a monoclinic structure at ambient conditions (space group $P2_1/c$, no. 14; see Fig. 1) [7]. The alkaline-earth metal (calcium) is bonded with eight oxygen atoms forming a CaO_8 polyhedron, while iodine is bonded with three oxygen atoms forming a triangular pyramid with short I-O bond distances ranging 1.7–1.9 Å. The CaO_8 polyhedron and IO_3 pyramid are bridged by sharing one oxygen atom between them. Along the b axis, there is an alternating arrangement of CaO_8 and IO_3 layers. Within the IO_3 layers, all the IO_3 units are oriented in different directions. It is this atomic arrangement which ultimately leads to the unexpected pressure-induced opening of the band gap of hydrated calcium iodate, which supports the model we previously developed to explain the band gap of metal iodates [4–6].

In this work, we report a pressure-induced nonlinear band-gap opening, from 4.52 eV at ambient pressure to 4.92 eV at 18.7 GPa, in hydrated calcium iodate, making it one of the widest band-gap metal iodates reported in the literature [4]. The band-gap behavior under compression is correlated with the pressure dependence of the I-O bond distance as determined from high-pressure powder x-ray diffrac-

tion measurements. These measurements, complemented with high-pressure Raman scattering experiments, have allowed us to identify two pressure-induced isostructural phase transitions that cause the nonlinear behavior of the band gap under compression.

II. METHODS

A. Sample synthesis

The single diffusion gel technique is found to be a simple strain free method for synthesizing single crystals with high purity, optical perfection, and wide morphology at room temperature. The gel having density 1.03 g/cm^3 was prepared by dissolving calcium nitrate tetrahydrate $\text{Ca}(\text{NO}_3)_2 \cdot 4\text{H}_2\text{O}$ in double distilled water. Potassium iodate having molarity 0.5 M is incorporated into the gel medium. The above prepared gel medium was acidified by adding glacial acetic acid to get the pH value 4.2. This acidified gel solution is transferred through the sides of the test tubes which is 20 cm in length and 2.5 cm in diameter to avoid the air bubbles inside the gel medium. These test tubes were kept undisturbed for three days to set the gel solution. Over this set gel 10 ml of 0.25 M calcium chloride solution was added. The test tubes were sealed to avoid contamination. This setup was kept undisturbed for the growth process to be completed. Hexagonal shaped white transparent good quality single crystals were obtained within one week. The fine powder sample was obtained by grinding a single crystal sample under a liquid medium (to obtain a smaller and more homogeneous particle size) with a mortar and pestle. To avoid contamination, we used the same liquid mixture used as pressure-transmitting medium in high-pressure experiments.

B. Optical absorption experiments at high pressure

A membrane-type diamond anvil cell was used to generate the high-pressure environments, and the culets of the diamond used in the diamond anvil cell were 400 μm in diameter. Stainless steel was used as the gasket material. The gasket was preindented to a thickness of 40 μm and a 200- μm hole, drilled in the center of the indentation area, served as the sample chamber. A single crystal sample, with a thickness of 10 μm , was selected and placed into the sample chamber together with a ruby sphere. A photograph of the loading at the lowest pressure can be found in the inset image of Fig. 2(a) in the main paper. The ruby fluorescence method was employed for the pressure calibration [8]. A mixture of methanol, ethanol, and water in a ratio of 16:3:1 was chosen as the pressure-transmitting medium, which can provide the hydrostatic conditions up to around 10 GPa [9].

The high-pressure optical absorption experiment was conducted in a bespoke optical system, which contains a mercury lamp (the range of the lamp is down to 220 nm), fused silica lenses, reflecting optics objectives, and a visible near-infrared spectrometer (Ocean Optics Maya2000 Pro). The sample-in and sample-out method was used to collect the absorption spectra, in which the intensity of the light transmitted through the sample $[I(\omega)]$ was normalized against the intensity

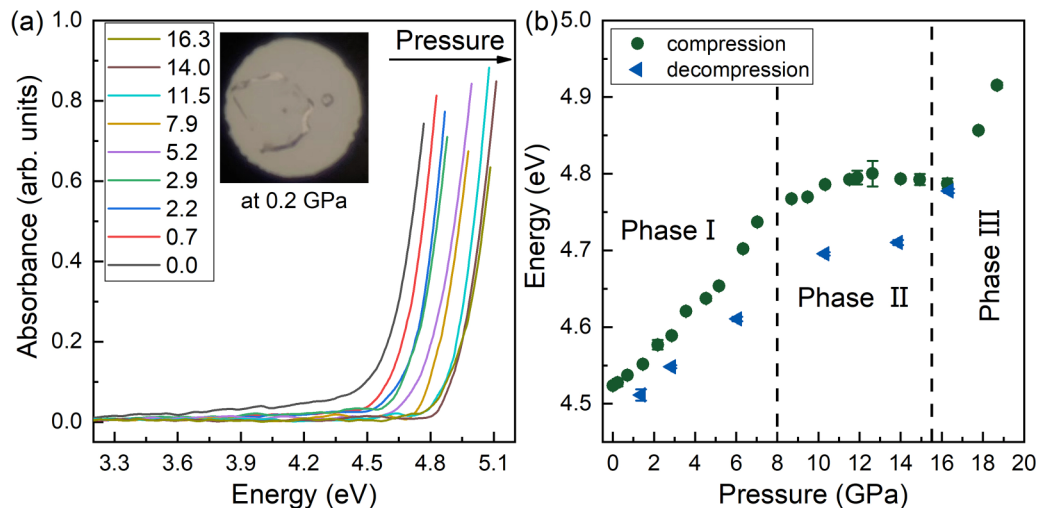


FIG. 2. (a) Optical-absorption spectra of $\text{Ca}(\text{IO}_3)_2 \cdot \text{H}_2\text{O}$ at selected pressures. The sample pressures associated with the spectra are shown in “GPa” in the legend. The inset shows the sample (large crystal) and the ruby chip (small crystal) inside the diamond anvil cell at 0.2 GPa. (b) The band-gap energy of $\text{Ca}(\text{IO}_3)_2 \cdot \text{H}_2\text{O}$ as a function of pressure, which was derived from the optical absorption spectra in (a) using Tauc plots. The band-gap evolution was divided into three regions based on the gradient of energy vs pressure. The vertical dashed lines indicate the transition pressures.

transmitted through an empty area in the pressure-transmitting medium [$I_0(\omega)$].

C. Powder x-ray diffraction experiments at high pressure

High-pressure angle-dispersive powder x-ray diffraction was performed at the BL04-MSPD beamline in ALBA-CELLS synchrotron [10]. A membrane-type diamond anvil cell was used to generate the high-pressure environment and the culets of the diamond were 500 μm . The preparation of the gasket used here is the same as that in the high-pressure optical absorption experiment. A mixture of methanol, ethanol, and water in a ratio of 16:3:1 was used as pressure-transmitting medium, a copper grain was loaded in the sample chamber with the powder sample, and the equation of state of copper was used as the pressure calibration [11]. The wavelength of the monochromatic x-ray beam was 0.4246 \AA , and the size of the beam spot is $20 \times 20 \mu\text{m}$ (full width at half maximum). The sample-to-detector distance was calibrated using a high purity LaB_6 powder, and the diffraction image was recorded with a Rayonix SX165 charge-coupled device detector. The diffraction image was integrated to the two-dimensional x-ray diffraction pattern by using the DIOPTAS program [12]. The Rietveld refinement of the powder pattern was performed in the FULLPROF suites [13].

D. Raman scattering experiments at high pressure

These experiments have been performed using a single crystal sample. A membrane-type diamond anvil cell with the diamond culets of 500 μm was used to generate the high-pressure environments. Here, the preparation of the gasket is the same as that in the high-pressure optical absorption experiment. A mixture of methanol, ethanol, and water in a ratio of 16:3:1 was used as pressure-transmitting medium, and the ruby fluorescence method was used as the pressure calibration [8]. A He/Ne laser with a wavelength of 632.8 nm

of 20 mW power was used as the light source and the microspectrometer was a HORIBA Jobin Yvon LabRAM HR UV model. A thermoelectrically cooled multichannel charge-coupled device detector with a resolution better than 2cm^{-1} was used to collect the signal. The setup was calibrated by helium plasma lines for the spectra in the ruby fluorescence region and silicon Raman-active modes for the Raman spectra region.

E. Calculation details

Ab initio simulations of $\text{Ca}(\text{IO}_3)_2 \cdot \text{H}_2\text{O}$ were calculated based on density function theory [14] as implanted in the Vienna *Ab initio* Simulation Package (VASP) [15] with the pseudopotential method according to the projector-augmented wave scheme [16] to treat the full nodal character of the all electron charge density in the core region. The basis set of the plane waves was extended with to a reasonable energy cut off 500 eV to achieve an accurate description of the electronic properties. The exchange-correlation interaction was considered in the generalized- gradient approximation, which is parametrized with the Perdew-Burke-Ernzerhof function [17]. For optimized configurations, the forces on the atoms were less than $0.0001 \text{eV \AA}^{-1}$, and it is worthwhile to note that all the simulations were performed at zero temperature ($T = 0$). In order to determine the interaction between different atoms, we calculated the crystal orbital overlap population by the Lobster code [18].

III. RESULTS AND DISCUSSION

A. Band-gap behavior under pressure

Figure 2(a) shows the absorption edge of $\text{Ca}(\text{IO}_3)_2 \cdot \text{H}_2\text{O}$. The measured absorption edge is sharper and has a weaker absorption tail than in our previous experiments in other iodates [4–6] because in the present study a single crystal was used for the measurements whereas in the previous experiments we used platelets obtained from

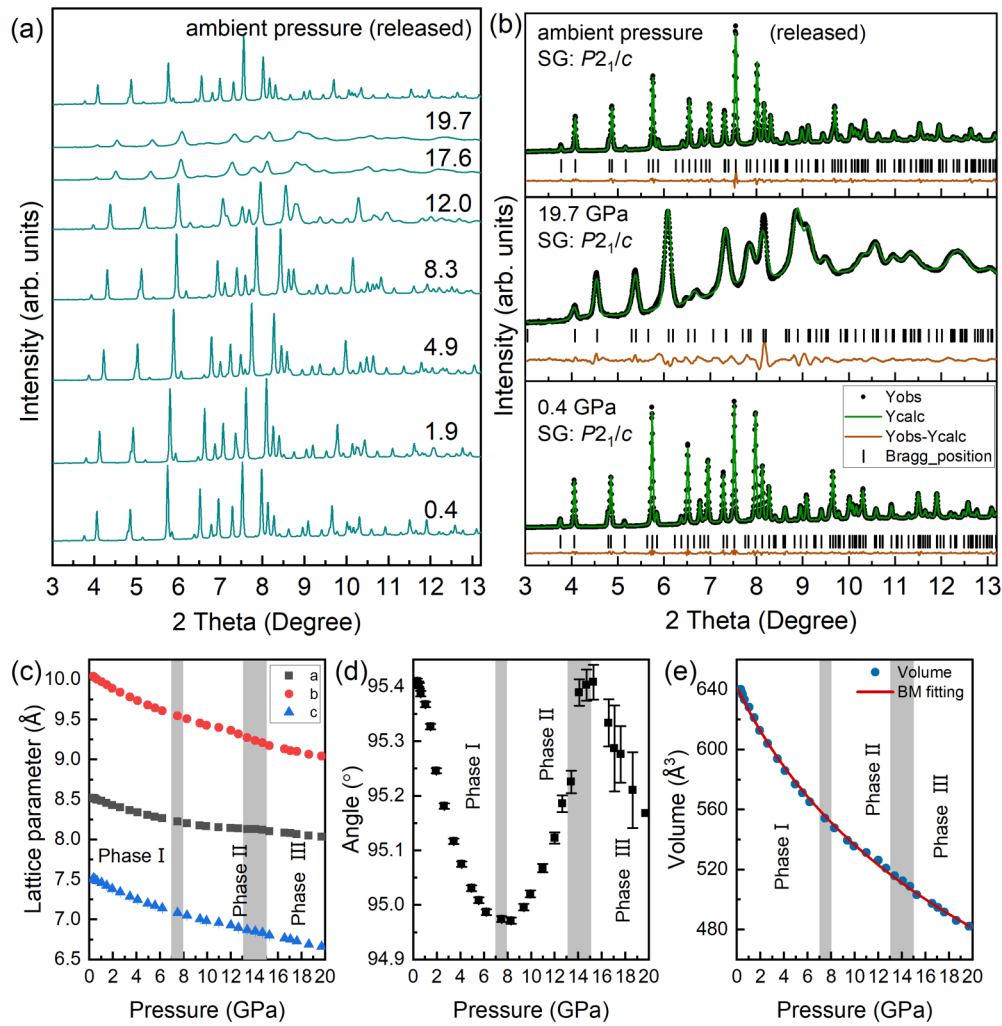


FIG. 3. (a) Powder x-ray diffraction patterns of $\text{Ca}(\text{IO}_3)_2 \cdot \text{H}_2\text{O}$ at selected pressures. Pressures are indicated in the right in “GPa”. (b) Rietveld refinements of the x-ray diffraction pattern at 0.4 GPa, 19.7 GPa, and ambient pressure after decompression. Experimental data (Y_{obs}), refined patterns (Y_{calc}), positions of diffraction peaks, and the residuals ($Y_{\text{obs}} - Y_{\text{calc}}$) are shown in black dots, green solid line, black ticks, and orange solid lines, respectively. “SG” is the space group of the crystal structure. (c)–(e) Lattice parameters, monoclinic angle, and unit-cell volume as a function of pressure. Gray regions indicate the pressure ranges in which the isostructural phase transitions occur. The red solid line is the Birch-Murnaghan (BM) fit of the unit-cell volume. In (c) and (e), error bars are smaller than symbols.

compressed powder. The absorption edge of $\text{Ca}(\text{IO}_3)_2 \cdot \text{H}_2\text{O}$ shows a blueshift under pressure [Fig. 2(a)], indicating a pressure-induced band-gap opening [Fig. 2(b)]. Our theoretical calculations of the electronic band structure (Fig. S1 in the Supplemental Material (SM) [19]) show that $\text{Ca}(\text{IO}_3)_2 \cdot \text{H}_2\text{O}$ is an indirect band-gap material at ambient pressure. Therefore, the Tauc plot for indirect band-gap materials was used (Fig. S2 in the SM [19]) to obtain the band-gap energy at each pressure [20]. The high-energy part of the $(\alpha h\nu)^{1/2}$ vs $h\nu$ has been fitted by a linear function and extrapolated to zero. α , h , and ν are the absorption coefficient, Planck’s constant, and the photon frequency, respectively. As plotted in Fig. 2(b), the band gap of $\text{Ca}(\text{IO}_3)_2 \cdot \text{H}_2\text{O}$ is 4.52 eV at ambient pressure and increases under compression to 4.70 eV at 7.9 GPa (phase I). Upon further compression the band-gap energy shows an almost pressure independent behavior up to 15.3 GPa (phase II). Finally, in phase III, the band-gap energy increases dramatically from 4.79 eV at 16.3 GPa up to

4.92 eV at 18.7 GPa. The band gap of diamond in the diamond anvil cell precluded acquisition of data at higher pressures [21]; however, based on the results shown in Fig. 2(b) and the crystal structure evolution, which we will show later, we expect the band gap of $\text{Ca}(\text{IO}_3)_2 \cdot \text{H}_2\text{O}$ to increase continuously and become larger than 5 eV above 20 GPa.

B. Crystal structure evolution under compression

Powder x-ray diffraction patterns of $\text{Ca}(\text{IO}_3)_2 \cdot \text{H}_2\text{O}$ collected at high pressure are shown in Fig. 3(a) up to 19.7 GPa. No extra reflections, reflection splitting, or disappearing reflections are observed over the whole pressure range. In fact, all patterns can be indexed with the original monoclinic $P2_1/c$ space group [7] as shown by the Rietveld refinements [13] of the representative powder x-ray diffraction patterns collected at the lowest pressure (0.4 GPa) and highest pressure (19.7 GPa) in Fig. 3(b). The pressure-induced changes of the

x-ray diffraction patterns are totally reversible upon sample decompression. The pattern collected after decompression [see Fig. 3(a)] and the Rietveld refinement [see Fig. 3(b)] support this conclusion. The quality factors of the Rietveld refinement are $R_p = 1.35\%$, $R_{wp} = 2.12\%$ (0.4 GPa), $R_p = 12.4\%$, $R_{wp} = 12.2\%$ (19.7 GPa), and $R_p = 1.15\%$, $R_{wp} = 1.71\%$ (ambient pressure released), respectively. All peaks shift to higher angles due to the contraction of the three lattice parameters [Fig. 3(c)] of the crystal structure under compression. At pressures higher than 12 GPa, the intensity of the peaks decreases dramatically, and the peaks become broadened, which is attributed to the gradual solidification of the pressure-transmitting medium used in the high-pressure experiment [9].

A monotonic decrease in the lattice parameters with small changes of slope as pressure increases are observed [Fig. 3(c)]. The changes of slope correlate with strong changes in the slope of the monoclinic angle at similar pressure regions [Fig. 3(d)]. In particular, the drastic slope changes occur in the pressure region of 7.0–8.0 GPa and 13.0–15.0 GPa. This can be interpreted because of the occurrence of two pressure-induced isostructural phase transitions. Similar pressure-induced isostructural transitions have been observed in other metal iodates, for instance, $\text{Fe}(\text{IO}_3)_3$ [22], $\text{Zn}(\text{IO}_3)_2$ [23], and $\text{Co}(\text{IO}_3)_2$ [24]. More evidence of the occurrence of the isostructural phase transitions can be found in the Raman spectra presented later. Notably, the pressures at which the slope changes in the lattice parameters and monoclinic angle happen agree with those at which changes happen in the band-gap energy. Here, following the name assignment used when describing the optical studies, we name the three phases as phases I, II, and III.

A second-order Birch-Murnaghan equation of state (wherein the pressure derivative of the axial linear modulus is fixed equal to 12.0) [25] as incorporated in EoSFit 7c [26] was used to fit the lattice parameters of phase I (Fig. S3 in the SM [19]). The zero-pressure value obtained from the fits for the three axes were $a_0 = 8.532(2)$ Å, $b_0 = 10.069(1)$ Å, and $c_0 = 7.545(1)$ Å. The axial linear moduli of the lattice parameters a , b , and c were 52.8(9), 33.2(2), and 26.5(2) GPa, respectively. This means that the most compressible axis is the c axis. Notably, the crystal structure of $\text{Ca}(\text{IO}_3)_2 \cdot \text{H}_2\text{O}$ shows a smaller anisotropic behavior than other metal iodates, such as $\text{Zn}(\text{IO}_3)_2$ [23], $\text{Co}(\text{IO}_3)_2$ [24], and $\text{Mg}(\text{IO}_3)_2$ [27]. We ascribe this feature to the different orientations exhibited by the IO_3 pyramids in $\text{Ca}(\text{IO}_3)_2 \cdot \text{H}_2\text{O}$. In the Zn, Co and Mg iodates, the IO_3 units are aligned in the same direction and there is a large gap between the $[\text{IO}_3]^-$ layers which is not exhibited in $\text{Ca}(\text{IO}_3)_2 \cdot \text{H}_2\text{O}$.

No apparent volume discontinuity occurs at the mentioned transition pressures in $\text{Ca}(\text{IO}_3)_2 \cdot \text{H}_2\text{O}$, as shown by the unit-cell volume obtained from the Rietveld refinements [Fig. 3(e)]. In fact, the combined data for all three phases can be described with a single third-order Birch-Murnaghan equation of state with a volume at zero pressure (V_0) of $641.8(5)$ Å³, a bulk modulus (B_0) of 39.0(7) GPa, and a pressure derivative (B'_0) of 4.0(1); i.e., the obtained equation of state is compatible with a second-order equation ($B'_0 = 4.0$). The bulk modulus is larger than those of $\text{Zn}(\text{IO}_3)_2$ (21.6 GPa) [23], $\text{Co}(\text{IO}_3)_2$ (29.8 GPa) [24], $\text{Mg}(\text{IO}_3)_2$ (22.2 GPa) [27],

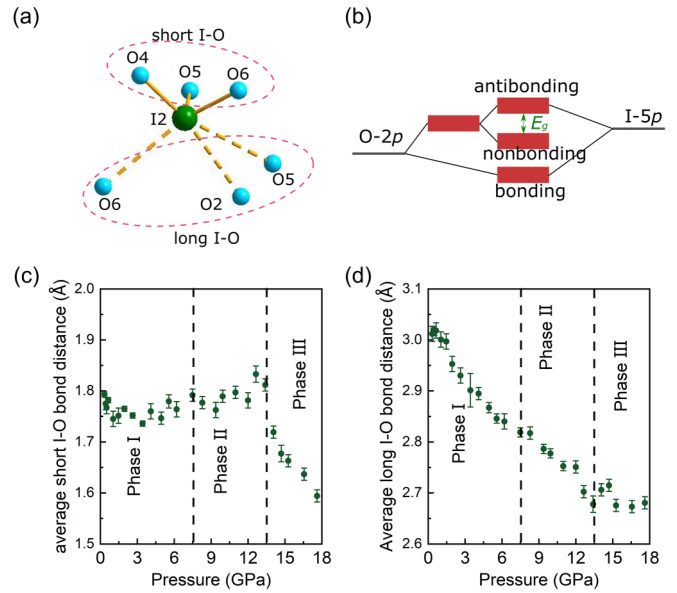


FIG. 4. (a) Representation of the IO_6 polyhedron. The solid bonds are the short I-O bonds that exist at ambient pressure, the dashed bonds are the long I-O distances that become bonds at high pressure. (b) Molecular orbital diagram near the Fermi level at ambient pressure. (c),(d) Pressure dependence of the average short I-O bond distances and average long I-O bond distances, respectively. All I-O distances are obtained from Rietveld refinements of powder x-ray diffraction patterns. The vertical dashed lines indicate the pressures at which slope changes are observed.

α - LiIO_3 (34 GPa) [28], and KIO_3 (24.3 GPa) [29], but smaller than that of $\text{Fe}(\text{IO}_3)_3$ (55 GPa) [28].

In order to determine the pressure dependence of the I-O distances, and to study their relation with the observed changes in the band gap, we have to consider that the iodine atoms are located at two different Wyckoff positions in the crystal structure of $\text{Ca}(\text{IO}_3)_2 \cdot \text{H}_2\text{O}$. For both iodine atoms, there are two types of I-O distances at ambient conditions [Fig. 4(a)]: (i) three short I-O distances in the range 1.7–1.9 Å that constitute the short I-O bonds that exist at room pressure and lead to threefold coordination of I atoms; (ii) three long I-O distances in the range 2.8–3.2 Å that do not form bonds at room pressure, but they do at high pressure and lead to a sixfold coordination of I atoms. Our previous studies on metal iodates showed that formation of the three long I-O bonds is a consequence of the presence of a lone electron pair in the iodine atom and that pressure helps to transform the lone electron pair into three additional bonds [5,22].

In $\text{Ca}(\text{IO}_3)_2 \cdot \text{H}_2\text{O}$, the average long I-O bond distance shortens under compression from the ambient pressure up to around 13.5 GPa and remains insensitive to pressure between 13.5 and 18 GPa [Fig. 4(d)]. On the other hand, the average short I-O bond distance shows a less sensitive behavior of pressure from the ambient pressure up to around 7.5 GPa (in this pressure range changes are comparable to error bars) and a slight increase in the pressure region of 7.5–13.5 GPa, which is followed by a considerable decrease between 13.5 and 18 GPa [Fig. 4(c)]. The slope changes observed in the average

long/short I-O bond distance occur at the same pressures as the slope changes in the band-gap energy [Fig. 2(b)] and the slope changes in the lattice parameters and monoclinic angle [Figs. 3(c) and 3(d)].

In order to correlate changes in the band gap and in the I-O bond distances, we have calculated the electronic density of states (DOS), the projected density of states (PDOS, Fig. S4 in the SM [19]), and the crystal orbital overlap population (Fig. S5 in the SM [19]) between the iodine atom (I2) and the six nearest oxygen atoms. In this way, we have been able to depict the molecular orbital diagram of $\text{Ca}(\text{IO}_3)_2 \cdot \text{H}_2\text{O}$ at ambient pressure (Fig. S6 in the SM [19]) and its detail near the Fermi level [Fig. 4(b)]. Since the observed phase transitions are isostructural, it is not expected that pressure would induce a substantial change in the topology of the band structure as was found in $\text{Fe}(\text{IO}_3)_3$ [5]. Therefore, the molecular orbital diagram can be used to explain not only the band gap at ambient pressure but also over the complete pressure range covered by our study, as seen in $\text{Mg}(\text{IO}_3)_2$ and $\text{Zn}(\text{IO}_3)_2$ [4]. The molecular orbital diagram near the Fermi level reflects that the band-gap energy is largely determined by the $p-p$ orbital interaction between iodine and oxygen atoms (the full discussion of the complete molecular orbital diagram of the interaction between iodine and oxygen can be found in the SM [19]). In particular, the valence band maximum in the electronic band structure is dominated by $\text{O}-2p$ nonbonding orbitals and the conduction band minima is dominated by antibonding $\text{O}-2p$ and $\text{I}-5p$ orbitals. This profile of the band structure is consistent with the common feature of the band structure for nontransition metal iodates [4,5]. In summary, the band gap of $\text{Ca}(\text{IO}_3)_2 \cdot \text{H}_2\text{O}$ is primarily determined by the energy difference between the $\text{O}-2p$ nonbonding state and the antibonding state of the $p-p$ interaction between iodine and oxygen atoms.

Since the pressure-induced opening or closing of the band gap is mainly related to the different shift rates of the conduction band minima with respect to the valence band maximum, the pressure dependence of the band gap is, to a first approximation, dominated by the behavior of the average distance of short I-O bonds under compression, since the interaction in the short I-O bonds is much stronger than that in the long I-O bonds (Fig. S5 in the SM [19]). The contribution of the change of the average distance of long I-O bonds under compression will, therefore, be of second order. However, if the short bonds are little affected by pressure, then a large change in length of the long I-O bonds will affect the behavior of the band-gap energy. Notice that, if the I-O bond distance shortens under compression, the hybridization of the $p-p$ interaction between iodine and oxygen is enhanced, increasing the separation between bonding and antibonding states, and thereby opening the band gap. In contrast, the expansion of the I-O bond distance will cause a decrease of the band-gap energy. In phase I of $\text{Ca}(\text{IO}_3)_2 \cdot \text{H}_2\text{O}$, the changes of the average short I-O distances are much smaller than in other iodates; indeed, changes are comparable to error bars [Fig. 4(c)]; i.e., they can be considered to remain nearly constant under pressure. Thus, the large decrease observed in the average long I-O distance [Fig. 4(d)] will cause the observed increase of the band-gap energy [Fig. 2(b)]. In phase II, the slight increase of the short I-O bond distance narrows the band-gap energy, compensated

by the effect from the shortening of the long I-O bonds. In summary, the band gap shows an independent behavior in this pressure region of phase II [Fig. 2(b)]. In contrast, in phase III, the short I-O bond distances decrease with increasing pressure [Fig. 4(c)] dominating the behavior of the band gap and causing a very rapid opening of the band-gap energy in this pressure region [Fig. 2(b)].

C. Evidence of the pressure-induced isostructural phase transition from Raman experiments

Finally, it should be stressed that Raman spectroscopy is an efficient tool for the detection of the local rearrangement of atoms and for the characterization of pressure-induced phase transitions [30,31]. The Raman spectra of $\text{Ca}(\text{IO}_3)_2 \cdot \text{H}_2\text{O}$ at selected pressures are plotted in Fig. 5(a). A waterfall plot of all the Raman spectra collected under high pressure could be found in Fig. S7 in the SM [19]. The Raman spectra collected at ambient pressure share the same features as in $\text{Zn}(\text{IO}_3)_2$ [23], $\text{Co}(\text{IO}_3)_2$ [24], and $\text{Mg}(\text{IO}_3)_2$ [27] and can be divided into three regions. The high-frequency region is located from 700 to 800 cm^{-1} and Raman modes in this region have been assigned to the symmetric and asymmetric stretching of $[\text{IO}_3]^-$ units [24,27]. The most intense peak is usually observed in this region [22–24,27]. The middle-frequency region is located between 300 and 400 cm^{-1} and Raman modes in this region are attributed to the symmetric and asymmetric bending of $[\text{IO}_3]^-$ units [24,27]. Finally, the low-frequency region is located below 300 cm^{-1} and the Raman modes of this region can be related to the translational and rotational motions of the iodate molecule as a rigid unit.

In Fig. 5(a), on increasing pressure, there is one Raman peak appearing at the lowest frequency in the high-frequency region if we compare the Raman spectra collected at ambient pressure and 3.3 GPa (it can be also observed in Fig. S8 in the SM [19]). These changes cannot be caused by a phase transition since no transition is detected by either of the other two diagnostic techniques used in this work. Actually, this vibrational mode exists at ambient pressure but it overlaps with the next Raman mode in the same region. The pressure dependence of this mode has been shown in a red triangle in Fig. S8 in the SM [19]. Therefore, the appearance of the new mode is related to the splitting of degenerate modes. Notice that, according to group theory, the studied compound has 72 Raman-active modes, however only 22 are observed at ambient pressure because of mode degeneracy. The splitting of modes is a typical phenomenon in compounds with anisotropic compressibility such as $\text{Ca}(\text{IO}_3)_2 \cdot \text{H}_2\text{O}$. Other changes, like the growing in intensity of some Raman modes in the middle- and low-frequency region, observed in this pressure range could be related to acquiring Raman spectra from parts of the sample with different orientations. Furthermore, the disappearance of some Raman peaks in the low- or high-frequency region is caused by merging with the neighboring peaks.

More intense extra Raman peaks appear at 6.6 GPa at both the high- and middle-frequency regions [see upward arrows in Fig. 5(a)]. Moreover, two Raman modes at around 750 cm^{-1} at ambient pressure show a totally different pressure coefficient before and after 6.6 GPa [Fig. 5(b) and Fig. S8 in

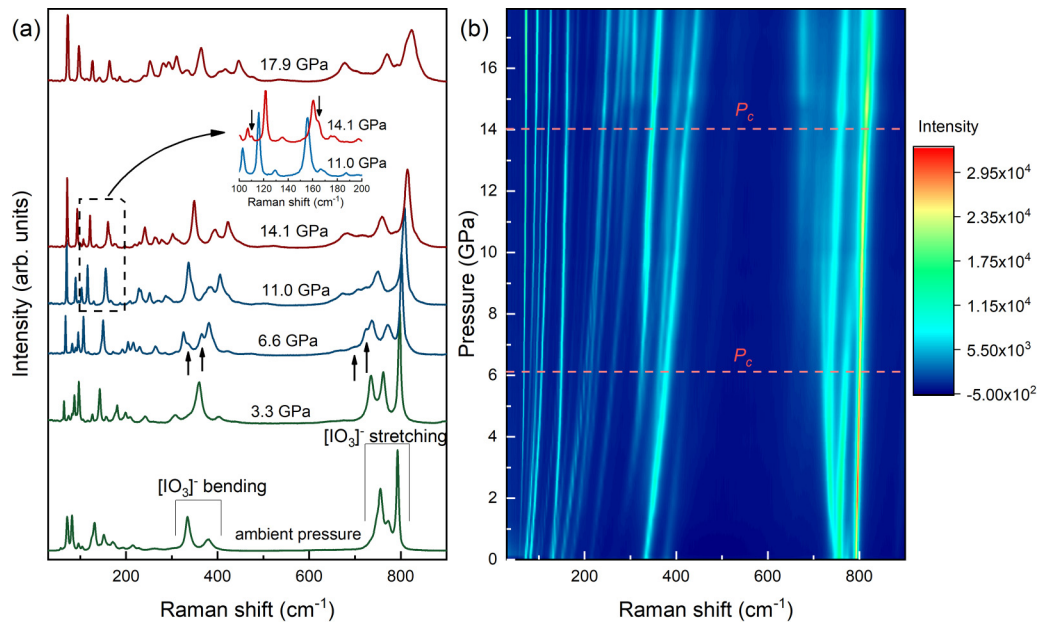


FIG. 5. (a) Raman spectra of $\text{Ca}(\text{IO}_3)_2 \cdot \text{H}_2\text{O}$ at selected pressures. The inset shows an enlarged representation of the area marked by a dashed square ($100\text{--}200\text{ cm}^{-1}$) for the Raman spectra collected at 11.0 and 14.1 GPa. Raman spectra of phases I, II, and III are shown in green, blue, and red, respectively. The upward and downward arrows indicate the appearance of the additional Raman peaks. (b) Contour plot of the Raman spectra collected at high pressure. The horizontal dashed lines labeled as “ P_c ” indicate the transition pressures.

the SM [19]]. All these changes confirm the first isostructural phase transition as we found in optical-absorption and x-ray diffraction experiments. Notice that the changes in the Raman spectrum are not caused by a decrease of the crystal symmetry (since the phase transitions are isostructural) but by local changes in the atomic coordination due to the anisotropic compressibility of the studied material. The changes in the high- and middle-frequency regions are related to the pressure-induced oxygen coordination increase of iodine. In particular, an increase of coordination usually leads to a decrease of the phonon gap between bending and stretching modes, as it happens for instance on the transition from scheelite to fergusonite [32]. Therefore, the extra modes of the high-frequency region with Raman shifts below 700 cm^{-1} are consistent with the increase of iodine coordination above 6 GPa. The emerging modes can be interpreted in this way: As the long I-O bond distances continuously shorten under compression and the stereo activity of the iodine lone electron pairs decreases, the iodine starts to gradually bond with the oxygen in the neighboring $[\text{IO}_3]^-$ units to form IO_6 units. Therefore, extra internal (both bending and stretching) modes of the IO_6 units appear in the middle- and high-frequency regions, respectively.

Additionally, some Raman mode splitting appears at 14.1 GPa [inset in Fig. 5(a)]. This fact coincides with the occurrence of the second pressure-induced isostructural phase transition. The reasons for changes in the Raman spectra are related to changes in the coordination of Ca and I and not to changes in the crystal symmetry. According to the x-ray diffraction experiments, the crystal symmetry does not change over the entire studied pressure range. The lowest energy Raman modes in the high-frequency region show a softening behavior in phases I and II, which can be observed in Fig. 5(b) and in Fig. S8 of the SM [19]. This is a result of a

slight enlargement of the short I-O bonds under compression since the frequency of the Raman modes correlates with the average I-O bond distance as observed in $\text{Zn}(\text{IO}_3)_2$ [23]. The pressure-induced changes in the Raman spectra are mostly reversible upon decompression (Fig. S7 [19]), however, upon compression a shoulder at the low energy side of the high-frequency region becomes more apparent than it initially was at ambient pressure. This mode existed at ambient pressure but overlapped with the neighboring Raman modes, and it becomes more apparent on decompression due to a slight hysteresis in the sample.

IV. CONCLUSIONS

The band-gap energy of $\text{Ca}(\text{IO}_3)_2 \cdot \text{H}_2\text{O}$ has been increased from 4.52 eV at ambient pressure up to 4.92 eV at 18.7 GPa, thus making this material one of the most transparent metal iodates reported in the literature. The successful engineering of the band-gap energy is attributed to the pressure-induced shortening of the average long or short I-O bond distances. We explain this phenomenon by building a molecular orbital diagram for $\text{Ca}(\text{IO}_3)_2 \cdot \text{H}_2\text{O}$ based on density-functional theory calculations. This model shows that the band-gap energy of $\text{Ca}(\text{IO}_3)_2 \cdot \text{H}_2\text{O}$ is dominated by the nonbonding $\text{O}-2p$ states and antibonding states of the $p-p$ interaction between I and O atoms. The band-gap energy and the I-O bond distance therefore exhibit an inverse relationship. The band gap also shows a nonlinear behavior under compression up to 18 GPa due to the existence of two pressure-induced isostructural phase transitions located at 6.6–8.0 GPa and 13.0–15.5 GPa, respectively, as evidenced by the nonlinear behavior of the lattice parameters and by the appearance of extra peaks in the Raman spectra. All changes of the structural, vibrational, and

optical properties were found to be reversible upon release of pressure.

ACKNOWLEDGMENTS

This study was supported by the MALTA Consolider Team network (Project No. RED2018-102612-T), financed by MINECO/AEI/0.13039/501100003329, the I+D+i Project No. PID2019-106383GB-41/42 financed by MCIN/AEI/10.13039/501100011033, as well as by the Projects No. PROMETEO CIPROM/2021/075 (GREENMAT) and No. MFA/2022/007 financed by Generalitat Valenciana. This study forms part of the Advanced Materials programme and was supported by MCIN with funding from European Union NextGenerationEU (PRTR-C17.I1) and by

Generalitat Valenciana. A.L. and D.E. thank the Generalitat Valenciana for Ph.D. Fellowship No. GRISOLIAP/2019/025. R.T. and D.E. thank the Generalitat Valenciana for Postdoctoral Fellowship No. CIAPOS/2021/20. The authors also thank ALBA synchrotron light source for the experiment funded under Proposal No. AV-2021095390 at the MSPD-BL04 beamline. J.S. and K.V. would like to acknowledge IIT Hyderabad for providing computational facilities. J.S. would like to acknowledge CSIR for his Ph.D. fellowship. G.V. would like to acknowledge the Institute of Eminence, University of Hyderabad (UoH-IoE-RC3-21-046) for funding and CMSD, University of Hyderabad, for providing computational facilities. The authors also thank the Tirant supercomputer (Universitat de Valencia) for providing computational resources.

- [1] H. Y. Chang, S. H. Kim, M. O. Kang, and P. S. Halasyamani, Polar or nonpolar? A^+ cation polarity control in $A_2Ti(IO_3)_6$ ($A = Li, Na, K, Rb, Cs, Tl$), *J. Am. Chem. Soc.* **131**, 6865 (2009).
- [2] C. F. Sun, C. L. Hu, X. Xu, J. B. Ling, T. Hu, F. Kong, X. F. Long, and J. G. Mao, $BaNbO(IO_3)_5$: A new polar material with a very large SHG response, *J. Am. Chem. Soc.* **131**, 9486 (2009).
- [3] J. Chen, C. L. Hu, F. F. Mao, X. H. Zhang, B. P. Yang, and J. G. Mao, $LiMg(IO_3)_3$: An excellent shg material designed by single-site aliovalent substitution, *Chem. Sci.* **10**, 10870 (2019).
- [4] A. Liang, R. Turnbull, P. Rodríguez-Hernandez, A. Muñoz, M. Jasmin, L. Shi, and D. Errandonea, General relationship between the band-gap energy and iodine-oxygen bond distance in metal iodates, *Phys. Rev. Mater.* **6**, 044603 (2022).
- [5] A. Liang, P. Rodríguez-Hernandez, A. Munoz, S. Raman, A. Segura, and D. Errandonea, Pressure-dependent modifications in the optical and electronic properties of $Fe(IO_3)_3$: The role of Fe 3d and I 5p lone-pair electrons, *Inorg. Chem. Front.* **8**, 4780 (2021).
- [6] A. Liang, F. Rodríguez, P. Rodríguez-Hernandez, A. Muñoz, R. Turnbull, and D. Errandonea, High-pressure tuning of $d-d$ crystal-field electronic transitions and electronic band gap in $Co(IO_3)_2$, *Phys. Rev. B* **105**, 115204 (2022).
- [7] E. Alici, T. Schmidt, and H. Lutz, Zur Kenntnis des Calciumbromats und -iodats, Kristallstruktur, roentgenographische, IR- und Raman-spektroskopische und thermo-analytische Untersuchungen, *Zeitschrift fuer Anorganische und Allgemeine Chemie* **608**, 135 (1992).
- [8] H. K. Mao, J. Xu, and P. M. Bell, Calibration of the ruby pressure gauge to 800 kbar under quasi-hydrostatic conditions, *J. Geophys. Res.* **91**, 4673 (1986).
- [9] S. Klotz, J. C. Chervin, P. Munsch, and G. Le Marchand, Hydrostatic limits of 11 pressure transmitting media, *J. Phys. D: Appl. Phys.* **42**, 075413 (2009).
- [10] F. Fauth, I. Peral, C. Popescu, and M. Knapp, The new material science powder diffraction beamline at alba synchrotron, *Powder Diffr.* **28**, 360 (2013).
- [11] A. Dewaele, P. Loubeyre, and M. Mezouar, Equations of state of six metals above 94 GPa, *Phys. Rev. B* **70**, 094112 (2004).
- [12] C. Prescher and V. B. Prakapenka, DIOPTAS: A program for reduction of two-dimensional x-ray diffraction data and data exploration, *High Press. Res.* **35**, 223 (2015).
- [13] J. Rodríguez-Carvajal, Recent advances in magnetic structure determination by neutron powder diffraction, *Phys. B (Amsterdam, Neth.)* **192**, 55 (1993).
- [14] P. Hohenberg and W. Kohn, Inhomogeneous electron gas, *Phys. Rev.* **136**, B864 (1964).
- [15] G. Kresse and J. Furthmüller, Efficient iterative schemes for ab initio total-energy calculations using a plane-wave basis set, *Phys. Rev. B* **54**, 11169 (1996).
- [16] P. E. Blöchl, Projector augmented-wave method, *Phys. Rev. B* **50**, 17953 (1994).
- [17] J. P. Perdew, K. Burke, and M. Ernzerhof, Generalized Gradient Approximation Made Simple, *Phys. Rev. Lett.* **77**, 3865 (1996).
- [18] S. Maintz, V. L. Deringer, A. L. Tchougréeff, and R. Dronskowski, LOBSTER: A tool to extract chemical bonding from plane-wave based DFT, *J. Comput. Chem.* **37**, 1030 (2016).
- [19] See Supplemental Material at <http://link.aps.org/supplemental/10.1103/PhysRevB.106.235203> for the description of the molecular orbital diagram, calculated electronic band structure, DOS, crystal orbital overlap population, experimental Raman spectra at all pressures, and pressure dependence of Raman modes.
- [20] J. Tauc, Optical properties and electronic structure of amorphous Ge and Si, *Mater. Res. Bull.* **3**, 37 (1968).
- [21] R. S. Balmer, J. R. Brandon, S. L. Clewes, H. K. Dhillon, J. M. Dodson, I. Friel, P. N. Inglis, T. D. Madgwick, M. L. Markham, T. P. Mollart, N. Perkins, G. A. Scarsbrook, D. J. Twitchen, A. J. Whitehead, J. J. Wilman, and S. M. Woollard, Chemical vapour deposition synthetic diamond: Materials, technology and applications, *J. Phys.: Condens. Matter* **21**, 364221 (2009).
- [22] A. Liang, S. Rahman, P. Rodríguez-Hernandez, A. Muñoz, F. J. Manjón, G. Nenert, and D. Errandonea, High-pressure raman study of $Fe(IO_3)_3$: Soft-Mode behavior driven by coordination changes of iodine atoms, *J. Phys. Chem. C* **124**, 21329 (2020).
- [23] A. Liang, C. Popescu, F. J. Manjon, A. Muñoz, Z. Hebboul, and D. Errandonea, Structural and Vibrational Study of $Zn(IO_3)_2$ combining high-pressure experiments and density-functional theory, *Phys. Rev. B* **103**, 054102 (2021).

- [24] A. Liang, C. Popescu, F. J. Manjon, R. Turnbull, E. Bandiello, P. Rodriguez-Hernandez, A. Muñoz, I. Yousef, Z. Hebboul, and D. Errandonea, Pressure-driven symmetry-preserving phase transitions in $\text{Co}(\text{IO}_3)_2$, *J. Phys. Chem. C* **125**, 17448 (2021).
- [25] F. D. Murnaghan, Finite deformations of an elastic solid, *Am. J. Math.* **59**, 235 (1937).
- [26] R. J. Angel, J. Gonzalez-Platas, and M. Alvaro, EosFit7c and a fortran module (library) for equation of state calculations, *Z. Kristallogr.* **229**, 405 (2014).
- [27] A. Liang, R. Turnbull, C. Popescu, F. J. Manjón, E. Bandiello, A. Muñoz, I. Yousef, Z. Hebboul, and D. Errandonea, Pressure-induced phase transition and increase of oxygen-iodine coordination in magnesium iodate, *Phys. Rev. B* **105**, 054105 (2022).
- [28] A. Liang, S. Rahman, H. Saqib, P. Rodriguez-Hernandez, A. Munoz, G. Nenert, I. Yousef, C. Popescu, and D. Errandonea, First-order isostructural phase transition induced by high pressure in $\text{Fe}(\text{IO}_3)_3$, *J. Phys. Chem. C* **124**, 8669 (2020).
- [29] L. Bayarjargal, L. Wiehl, A. Friedrich, B. Winkler, E. A. Juarez-Arellano, W. Morgenroth, and E. Haussühl, Phase transitions in KIO_3 , *J. Phys.: Condens. Matter* **24**, 325401 (2012).
- [30] R. Turnbull, M. E. Donnelly, M. Wang, M. Peña-Alvarez, C. Ji, P. Dalladay-Simpson, H. K. Mao, E. Gregoryanz, and R. T. Howie, Reactivity of Hydrogen-Helium and Hydrogen-Nitrogen Mixtures at High Pressures, *Phys. Rev. Lett.* **121**, 195702 (2018).
- [31] P. Dalladay-Simpson, R. T. Howie, and E. Gregoryanz, Evidence for a new phase of dense hydrogen above 325 gigapascals, *Nature (London)* **529**, 63 (2016).
- [32] D. Errandonea, F. J. Manjón, A. Muñoz, P. Rodríguez-Hernández, V. Panchal, S. N. Achary, and A. K. Tyagi, High-pressure polymorphs of TbVO_4 : A Raman and ab initio study, *J. Alloys Compd.* **577**, 327 (2013).